ENHANCED HEAT TRANSFER UNDER THE INFLUENCE OF COHERENT STRUCTURE INDUCED BY ARC VORTEX GENERATOR IN SQUARE PIPE FLOWS

by

Wei WANG[a], Xiao-Jiao SUN[a], Yang GAO[a], Xin-Lei GUAN[a], Chu-Wen GUO[a], Li-Jun WANG[a] *

[a] School of Electrical and Power Engineering, China University of Mining and Technology, Xuzhou 221008, China

Experiments and numerical simulations were both performed to investigate coherent structures and heat transfer process in a square pipe turbulent flows induced by arc vortex generator (AVG). The velocity fields of induced turbulent flow was obtained by planar particle image velocimetry (PIV). The analysis of velocity profiles revealed the co-existence of various coherent structures (CS). Turbulent fluctuation quantities, such as turbulent intensities, Reynolds stress, etc. exhibited the different behaviors of fluid motions introduced by AVG. Probability density function (PDF) of swirling strength showed the complication of the vortex-rotating. Heat transfer process was simulated using large eddy simulation (LES). The results of Nusselt number (Nu) achieved the maximal improvement 57% with the use of AVG. The distribution of Nu was in good agreement with the distribution of CSs, especially hairpin vortices and subsequent secondary CS, which highlighted the influence of CSs generated by AVG on heat transfer enhancement.

Key words: *vortex generator, coherent structure, heat transfer enhancement*

Introduction

Heat transfer enhancement is very important to modern industrial process such as heat exchangers and refrigeration systems. Researchers put forward lots of techniques[1, 2] to improve heat transfer efficiency, which include vortex generator (VG). Planar or solid VGs[3, 4] are frequently applied due to its simple form and low cost. VG induces secondary flows which lead to coherent structures (CS), like counter-rotating vortices pair (CVP) and hairpin vortices, and indirectly enhances heat transfer through CSs[5]. The study of VG needs more details about the development and interaction of CSs for understanding the mechanism of heat transfer enhancement.

Early researches[5, 6] highlighted the function of the longitudinal CVP in VG flows. Some studies[7, 8] mentioned the generation of hairpin vortices on the upper edge of VG. Meng *et al.*[8, 9] both experimentally and numerically investigated the flows associated with a trapezoidal-shaped VG and confirmed the co-existence of CVP and hairpin vortices. Habchi *et al.*[10]

* Corresponding author ; e-mail: lj_wang1@126.com

investigated twelve configurations of VGs and found the interactions of CSs greatly enhances the heat transfer. Hamed *et al.*[10] analyzed the influences of VG's geometry and incoming flow on the CSs and flow state. They found the generations of hairpin vortices happened more early with increasing Reynolds number (Re). Oneissi *et al.*[11] compared the global performances of winglet VGs with and without hemispheric protrusion. Their results showed with the interaction between hairpin vortices introduced by hemispheric protrusion and CVP by winglet VG, the heat transfer can be improved 7% more than using winglet VG only. There were more and more evidence for the importance of hairpin vortices induced by VG. In this study, we focus on the role of hairpin vortices and reveal the relationship of hairpin vortices with heat transfer.

In this study, the flow field with arc VG (AVG) was measured by planar PIV and the heat transfer process was obtained by numerical simulations with LES model. The experimental setup and numerical methods were firstly introduced. Then the fluid motions including fluctuating quantities were compared and analyzed. Finally the heat transfer performance with AVG were discussed combined with the influence of CSs.

Experimental setup and numerical method

The experiment was conducted in a Plexiglas square pipe with 300 mm length and 20 mm side, shown in Fig. 1. The *x*-axis is the flow direction, the *y*-axis is the wall normal direction and the z-axis is the transverse direction. The AVG had a 45° inclined angle, the height H=3.5 mm, the 4 mm width, the 6 mm curvature radius of the upper edge and the 2 mm thickness. The model was mounted in the center transverse plane at x_0=170 mm from the inlet of the pipe. Planar PIV was used for the acquisitions of the velocity fields in the streamwise-wall normal plane. A time-series of 9700 snapshots were recorded by an OLYMPUS I-speed 3 camera with a resolution of 2048×2048 pixels at sampling rate 2000 Hz. The image pairs were processed using adaptive correlation algorithm with an interrogation window of 16×16 pixels, a 50% overlap rate, resulting in the velocity fields of 159×27 vectors with a 0.5125 mm spacing in both directions. Re_h is 3546 based on the height H and the freestream velocity $U_\infty = 1\, m/s$.

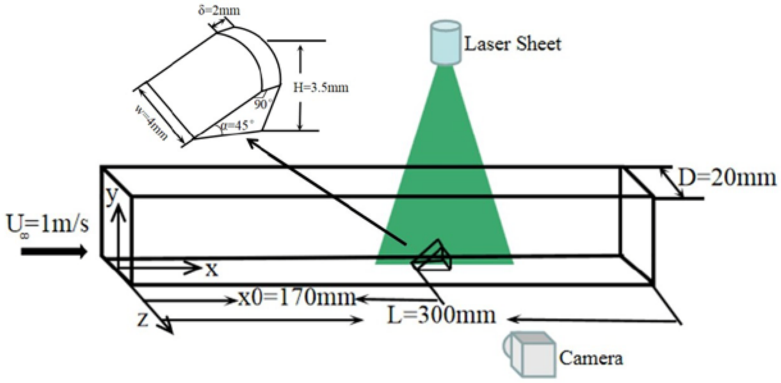

Fig.1 Experimental setup and AVG model

The disturbed turbulent flows were carried out by ANSYS Fluent 17.0 code with Large Eddy Simulation (LES) model to give more information about the heat transfer process. In this study, numerical simulations included two parts: (1) water was chosen as the fluid material to compare with the results of the experiment and verify the LES model. The physical parameters of water were the density ρ=1000 kg/m^3, the thermal conductivity k=0.599 W/(m·K), specific heat capacity C_p=4.186

kJ/(kg·K), the dynamic viscosity μ=1.004×10^{-3} Pa·s; (2) due to the Prandtl number (*Pr*) of water was 7 which means the transport of momentum is more faster than the transport of temperature in water, we used the air whose *Pr* is 0.7 for the simulation of heat transfer process instead of water. The physical parameters of air are ρ=1.205 kg/m^3, k=0.023 W/(m·K), C_p=1.013 kJ/(kg·K), μ=1.81×10^{-5} Pa·s. All the flow environments were remained as the above experiment except for the freestream velocity increase to 7 m/s for the approximation of *Re*.

The continuity, momentum and energy equations in numerical simulations were as follow:

$$\frac{\partial \rho u_i}{\partial x_i} = 0 \tag{1}$$

$$\frac{\partial \rho u_i}{\partial t} = -\frac{\partial p}{\partial x_i} + \frac{\partial}{\partial x_i}\left(\mu \frac{\partial u_i}{\partial x_j} - \rho \overline{u_i' u_j'} \right) - \frac{\partial \rho u_i u_j}{\partial x_j} \tag{2}$$

$$\frac{\partial \rho T}{\partial t} + \frac{\partial \rho u_i T}{\partial x_i} = \frac{\partial}{\partial x_i}\left(\frac{k}{C_p} \frac{\partial T}{\partial x_i} \right) \tag{3}$$

where u_i was instantaneous velocities, x_i was the coordinates, p was pressure, t was time, u_iu_j was Reynolds stress, and T was temperature.

The SIMPLE algorithm and QUICK scheme were used for the coupling of velocity and pressure and the convection terms, respectively. The second-order upwind scheme was used to discretize the convection term. The residuals were set to less than 10^{-6} for the energy equation and 10^{-4} for other variables. The time step was 0.1 ms for the convergence. The Smargorinsky-Lily sub-grid model was selected in LES model. The flow in the vicinity of the wall was dealt with the enhanced wall function. Non-slip condition was applied to all the solid surfaces in the simulations.

The Reynolds number *Re* is defined as:

$$Re_h = \frac{\rho u_b H}{\mu} \tag{4}$$

where u_b is the bulk fluid velocity.

The Nusselt number *Nu* is described as：

$$Nu = \frac{h_0 D}{k} \tag{5}$$

where D was the equivalent diameter, and the heat transfer coefficient h_0 was defined as：

$$h_0 = \frac{q_w}{T_w - T_f} \tag{6}$$

where q_w was the heat flux, T_w was the temperature on the surface of the pipe and set to 343K, T_f was the mean temperature of the bulk fluid and calculated as $T_f = \left(T_{in} + T_{out}\right)/2$ where T_{in} was the inlet temperature and set to 293K, T_{out} is the outlet temperature. The analyzed *Nu* in this study was area-averaged as:

$$Nu = \frac{1}{A}\int_A Nu_x dA \tag{7}$$

where the subscript x denoted the quantity in the streamwise direction, A was the area of the cross-section.

The computational domain was discretized into a structured mesh and a very fine and 5 grid quantities, 1.1 million, 2.2 million, 3 million, 4.1 million, and 5.2 million, were used to test the grid independence. LES simulation required the normalized vertical coordinate y^+ of the first point away from the wall must be less than 1. From Table 1, when the grid quantity was larger than 3 million, the $y^+<1$ condition can be satisfied. After the grid quantity exceeded 4.1 million, the changes of Nu in computational flows was less than 0.5% which can be considered as the convergence. Therefore, in this study the grid number is set to be 4.1 million.

Table 1. The y^+ value of the first point away from the wall with different grid numbers

Grid quantities	1146564	2238568	3001348	4067588	5217740
y^+_{min}	3.74	1.25	0.65	0.62	0.59

Results and discussion

Turbulent flows induced by AVG

Fig. 2 gave the developments of the mean streamwise velocity profiles along the *x* direction in the streamwise-wall normal plane. The grey block denoted the AVG, the red line denoted the LES results and the black circle denoted the PIV results. Velocity profiles from LES were in good agreement with the PIV measurement in all x locations, which validated the reliability of LES simulation. The development of the shear layer[8] on the upper edge of AVG at *y*=1H can be well captured by LES. The variation tendencies of LES profiles in y direction at each x location were also consistent with PIV profiles. In fact, due to the 5 times higher spatial resolution of LES than PIV in this study, near-wall region flows underneath y=0.5H were more obvious for the LES results.

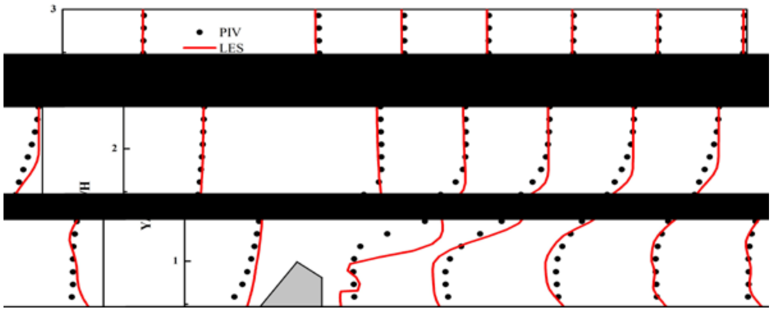

Fig. 2 The developments of mean streamwise velocity profiles along the x-direction in the streamwise-wall normal plane from PIV and LES data

Fig. 3 showed the distributions of inflection points ($\partial u/\partial y = 0$) and indent points ($\partial^2 u/\partial y^2 = 0$) calculated from more velocity profiles in Fig. 2. There was two-layer alternating distributions of "inflection point-indent point-inflection point-indent point". The upper layer reflected the existence of heads of primary hairpin vortices shed from the upper edge of AVG and induced secondary vortices. Meanwhile the lower layer represented the existence of CVP and corresponding secondary vortices[9]. The linear-fitting lines from the distributions of both points were displayed in Fig. 3 as solid and dash lines, respectively. The slopes of these lines indicated the upward motions of CSs during they moved downstream. Table 2 listed the fitted expressions of inflection points from two layers and corresponding inclined angels. Due to the limitation from upper hairpin vortices at higher locations, the lifting of the lower CVP is about half of the former.

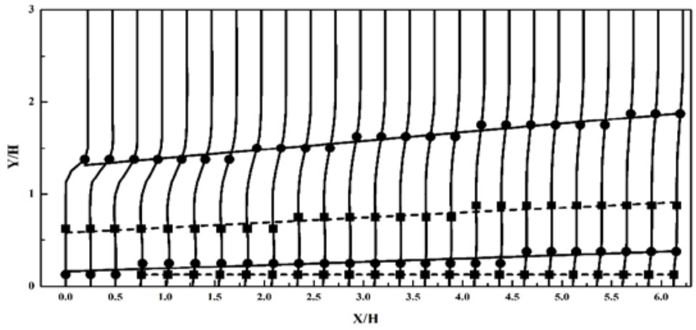

Fig.3 The distributions of inflection points (●) and indent points (■) in the mean streamwise velocity profiles. The solid lines and dash lines denote the corresponding fitted curves of both points.

Table 2. Fitted expressions and inclined angels of inflectional points from two layers

	Fitted expression	Inclined angel
Upper inflection points	*y=0.15x+0.70*	8.3
Lower inflection points	*y=0.07x+0.82*	3.9

Fig. 4 a and b showed the distributions of the streamwise and wall normal turbulent intensities, *Tu* and *Tv* in the x-y plane, respectively. The fluid motions in x and y directions introduced by AVG had different distributions: *Tu* had two extreme area, corresponding to the regions of hairpin vortices and CVP, respectively. In contrast, *Tv* only had one extreme area, locating between the regions of CSs. It was implied that streamwise fluctuation may come from the CS individually while vertical fluctuation comes from the interaction of CSs. Fig. 4 c showed the distribution of Reynolds stress $-\overline{u'v'}$ which exhibits a clear alternation of positive and negative values. The periodic distribution confirmed the importance of hairpin vortices in the momentum transport of the turbulent flows with AVG[16, 17]. Fig. 4 d gave the distribution of turbulent kinetic energy (TKE) which is similar to the contour of *Tu* because of its higher value.

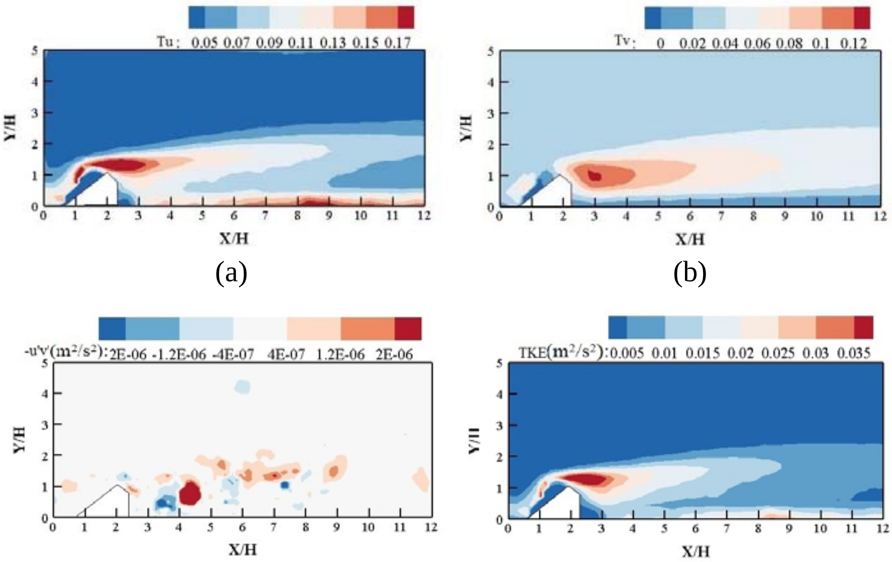

(a) (b)

(c) (d)

Fig.4 (a) streamwise turbulent intensity *Tu*; (b) wall normal turbulent intensity *Tv*; (c) Reynolds stress $-\overline{u'v'}$; (d) turbulent kinetic energy (TKE) in the streamwise-wall normal plane*Heat transfer performance associated with CSs*

Fig. 5 a and b displayed the distributions of probability density functions (PDFs) of positive vortex and negative vortex, respectively. The vortex were identified by swirling strength λ_{ci} [18-20] and multiplied by the sign of transverse vorticity for distinguishing the rotating directions. The black line in Fig. 5 b, indicating the locations of PDF extreme of negative vortex, i.e. counterclockwise-rotating vortex, with a 8° inclined angel, coincided with the upper inflection points line in Fig. 3, which indicated the dominant contribution of hairpin vortices to negative vortex. PDF extreme of positive vortex happened on both sides of the extreme of negative vortex, revealing the rotation-reversing relationship between the primary CSs and induced secondary CSs.

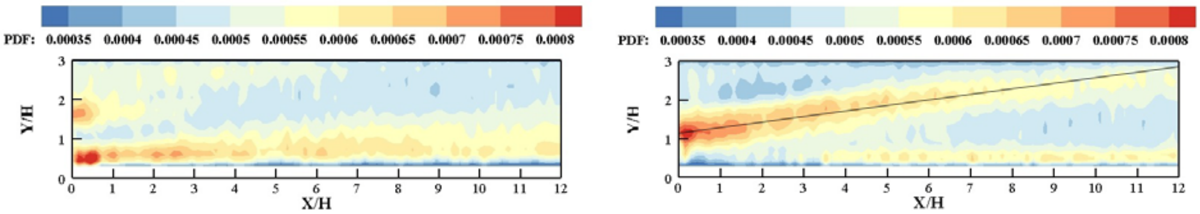

(a) positive vortex (b) negative vortex

Fig.5 The distributions of normalized probability density functions (PDFs) of (a) positive vortex and (b) negative vortex

Fig. 6 displayed the instantaneous distributions of temperature T in the cross-section at x=0.5H-5.5H with 0.5H interval. The contours vividly revealed the influence of CSs on the heat transfer process. In the near-wake region just behind AVG, shown in Fig.6 a and b, the heat flux was carried by the rising fluid and had a "mushroom" shape which was consistent with the cross-section of hairpin vortices, indicating the significant contribution to the heat transport, especially above the upper half of AVG. The range and strength of heat flux vanished after x=5.5H due to the decay of CSs.

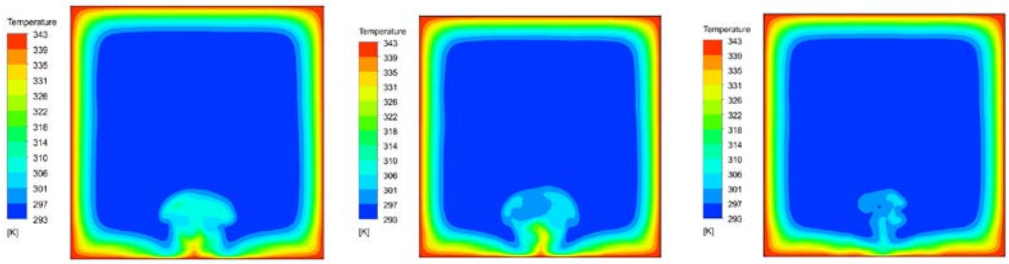

(a) x=0.5H (b) x=1.5H (c) x=2.5H

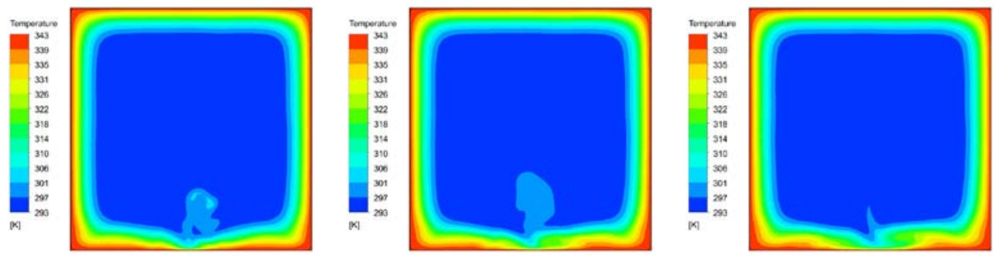

(d) x=3.5H (e) x=4.5H (f) x=5.5H

Fig. 6 The distributions of temperature T in the cross-section at x= (a) 0.5H, (b) 1.5H, (c) 2.5H, (d) 3.5H, (e) 4.5H, and (f) 5.5H

Fig. 7 gave the results of Nu along the x-direction in the flows with and without AVG, and the latter's result was denoted by the subscript 0. Here Nu was area-averaged within the cross-section, resulting in the variation of Nu only in the x-direction. It was highlighted the improvement of heat transfer with the use of AVG compared to the case without AVG. The intense heat transfer enhancement, approaching 57%, happened 1H ahead of and 2.5H behind the AVG while the heat transfer was still augmented but with a mild degree further downstream.

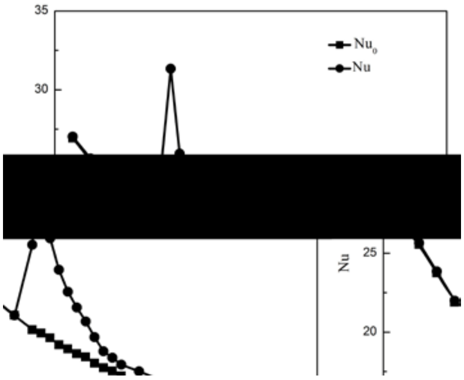

Fig. 7 The distributions of *Nu* along the streamwise direction in the flows with and without AVG

Fig. 8 further revealed the close relationship between the distribution of *Nu* and CSs. The upper figure was Nu and the lower figure was the 3-dimensional CSs from the top view. The pink surfaces denoted the λ_{ci}-identified CSs, basically a train of hairpin vortices shed from the upper edge of AVG, which surrounded a pair of counter-rotating quasi-streamwise vortices, visualizing as the red and blue surfaces, respectively. The range of enhanced heat transfer was closely associated with the distributions of CSs. Both had the similar width which reached normalized transverse length L_z^+=3 downstream. Ahead of x=2H, the contour of *Nu* had two-branches like CSs in this region.[15] The results revealed the dominance of CSs on the heat transfer process, which means the improvement of heat transfer performance come down to the control problem of CSs generated by AVG.

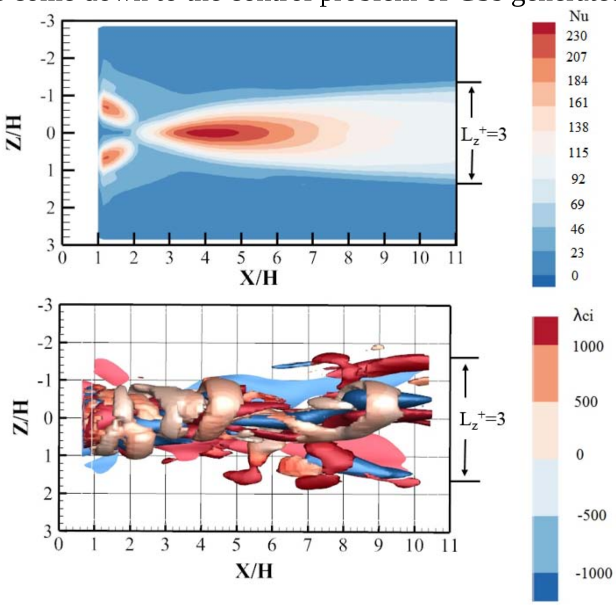

Fig. 8 The relationship between the distributions of *Nu* and CSs generated by AVG

Conclusion

Experimental measurement and numerical simulations were performed in square pipe flows with AVG. The turbulent flows induced by AVG and subsequent heat transfer performance were analyzed. The velocity profiles and fluctuation quantities exhibited the existence of CSs generated by AVG and accompanying disturbances to the original flow. The Nu of the turbulent flow can be improved 57% with the use of AVG. And the enhanced heat transfer was attributed to the dominant control of CSs, especially hairpin vortices and related secondary CSs.

Acknowledgement

This work was supported by the National Science Foundation of China (11802331) and the Frontier Science Research Project (Grant No. 2017XZKD02) in the China University of Mining and Technology.

Nomenclature

H—arc vortex generator height,[mm]	h_0—heat transfer coefficient,[W/(m^2•K)]
U_∞—freestream velocity,[m/s]	D—equivalent diameter,[mm]
ρ—density,[kg/m^3]	Tu—streamwise turbulent intensity
k—thermal conductivity, [W/(m•K)]	Tv—wall normal turbulent intensity
C_p—specific heat capacity, [kJ/(kg•K)]	$-\overline{u'v'}$ —Reynolds stress, [m^2/s^2]
μ—dynamics viscosity, [kg/(m•s)]	λ_{ci}—swirling strength

References

[1] Chang, S.W., *et al.*, Influence of spiky twisted tape insert on thermal fluid performances of tubular air–water bubbly flow. *International Journal of Thermal Sciences*, 48 (2009), pp. 2341-2354.

[2] Liu, P., *et al.*, Numerical study on characteristics of heat transfer and friction factor in a circular tube with central slant rods. *International Journal of Heat and Mass Transfer*, 99 (2016), pp. 268-282.

[3] Wu, J.M., Tao, W.Q., Numerical study on laminar convection heat transfer in a channel with longitudinal vortex generator. Part B: Parametric study of major influence factors. *International Journal of Heat and Mass Transfer*, 51 (2008), pp. 3683-3692.

[4] Wu, J.M., Tao, W.Q., Effect of longitudinal vortex generator on heat transfer in rectangular channels. *Applied Thermal Engineering*, 37 (2012), pp. 67-72.

[5] Biswas, K., *et al.*, Numerical and experimental determination of flow structure and heat transfer effects of longitudinal vortices in a channel flow. *International Journal of Heat and Mass Transfer*, 39 (1996), pp. 3441–3451.

[6] Esmaeilzadeh, A., *et al.*, Comparison of simple and curved trapezoidal longitudinal vortex generators for optimum flow characteristics and heat transfer augmentation in a heat exchanger. *Applied Thermal Engineering*, 125 (2017), pp. 1414-1425.

[7] Lögdberg, O., *et al.*, Streamwise evolution of longitudinal vortices in a turbulent boundary layer. *Journal of Fluid Mechanics*, 623 (2009), pp. 27-56.

[8] Yang, W., *et al.*, Dynamics of hairpin vortices generated by mixing tab in a channel flow. *Experiments in Fluids*, 30 (2001), pp. 705-722.

[9] Dong, S., Meng, H., Flow past a trapezoidal tab. *Journal of Fluid Mechanics*, 510 (2004), pp. 210-242.

[10] Habchi, C., *et al.*, Bougeard D., Hachem F., Elmarakbi A., Chaotic mixing by longitudinal vorticity. *Chemical Engineering Science*, 104 (2013), pp. 439-450.
[11] Hamed, A.M., *et al.*, Vortical structures in the near wake of tabs with various geometries. *Journal of Fluid Mechanics*, 825 (2017), pp. 167-188.
[12] Oneissi, M., *et al.*, Heat transfer enhancement of inclined projected winglet pair vortex generators with protrusions. *International Journal of Thermal Sciences*, 134 (2018), pp. 541-551.
[13] Webb, R.L., Performance Evaluation Criteria for Use of Enhanced Heat Transfer Surfaces in Heat Exchanger Design. *International Journal of Heat and Mass Transfer*, 24 (1981), pp. 715-726.
[14] Asai, M., Nishioka, M., Boundary-layer transition triggered by hairpin eddies at subcritical Reynolds numbers. *Journal of Fluid Mechanics*, 297 (1995), pp. 101-122.
[15] Elavarasan, R., Meng H., Flow visualization study of role of coherent structures in a tab wake. *Fluid Dynamics Research*, 27 (2000), pp. 183-197.
[16] Adrian, R., *et al.*, Vortex organization in the outer region of the turbulent boundary layer. *Journal of Fluid Mechanics*, 422 (2000), pp. 1-54.
[17] Adrian, R., Hairpin vortex organization in wall turbulence. *Physics of Fluids*, 19 (2007), 041301.
[18] Jeong, J., Hussain F., On the identification of a vortex, *Journal of Fluid Mechanics*, 285 (1995), pp. 69-94.
[19] Chakraborty, P., *et al.*, On the relationships between local vortex identification schemes. *Journal of Fluid Mechanics*, 535 (2005), pp. 189-214.
[20] Zhou, J., *et al.*, Mechanisms for generating coherent packets of hairpin vortices in channel flow. *Journal of Fluid Mechanics*, 387 (1999), pp. 353-396.

Paper submitted: June 5, 2018
Paper revised: August 6, 2018
Paper accepted: November 1, 2018